# Lab on a Chip

Accepted Manuscript

This is an *Accepted Manuscript*, which has been through the Royal Society of Chemistry peer review process and has been accepted for publication.

Accepted Manuscripts are published online shortly after acceptance, before technical editing, formatting and proof reading. Using this free service, authors can make their results available to the community, in citable form, before we publish the edited article. We will replace this *Accepted Manuscript* with the edited and formatted *Advance Article* as soon as it is available.

You can find more information about *Accepted Manuscripts* in the **Information for Authors**.

Please note that technical editing may introduce minor changes to the text and/or graphics, which may alter content. The journal's standard **Terms & Conditions** and the **Ethical guidelines** still apply. In no event shall the Royal Society of Chemistry be held responsible for any errors or omissions in this *Accepted Manuscript* or any consequences arising from the use of any information it contains.
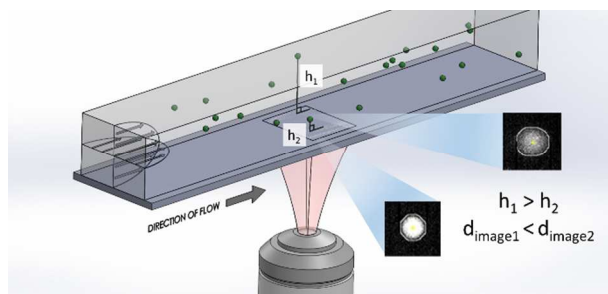
This work represents the first implementation of a defocusing-based three-dimensional (3D) particle tracking technique for microfluidic particle focusing applications.

Lab on a Chip

Application of a three-dimensional (3D) particle tracking method to microfluidic particle focusing

Michael H. Winer[a], Ali Ahmadi[b] and Karen C. Cheung[a]

In this paper, a defocusing-based three-dimensional (3D) particle tracking method is presented and demonstrated for microfluidic particle focusing applications. Previous work in particle focusing has verified particle position in two dimensions (2D) using micro-streak velocimetry, or confocal and stereoscopic setups for 3D tracking. The results obtained from the methodology presented are compared with the theoretical and previously observed trends, and it is shown that the defocusing technique provides a simple and precise tool for determining the 3D locations of cell-sized particles in microscale flows (Re ≤ 100). Although similar methods exist for micro-particle image velocimetry (μ-PIV) applications, this is the first implementation of this technique for particle focusing applications.

1. Introduction

Particle tracking techniques have become an essential tool for characterizing microfluidic systems for lab on a chip applications. In recent years, numerous 2D and 3D methods have been developed to obtain the flow field and particle position in microfluidic channels. 2D particle tracking based on tracking individual fluorophores has been developed mainly for applications related to μPIV[1-4]. Fluorescence imaging can be used to track individual fluorophores in 2D sub-nanometre accuracy[5]. Although these 2D techniques are simpler to implement, 3D tracking is required in some microfluidic applications including characterization of micro-mixers or particle focusing devices.

To address the limitations of 2D approaches, several 3D tracking techniques have been introduced including single camera (e.g. confocal scanning microscopy, anamorphic/astigmatic imaging, digital holographic microscopy, deconvolution microscopy) and multi-camera (e.g. stereoscopic imaging, tomographic imaging) approaches[6-14]. Recent review articles have described advantages and disadvantages of each of these methods in detail[15-17]. These techniques have been successfully used to track the 3D path of particles as small as 100 nm with high accuracy[18-22]. However, several of these methods require expensive and intricate optical setups involving numerous lenses, cameras, aperture designs, and light sources. Astigmatic particle image velocimetry (APTV) is perhaps the simplest in experimental design, and has been used to determine particle positions in acoustophoretic devices[23, 24]. However, work with APTV thus far has not include high-Re flow profiles[25].

In recent years, inertial focusing as a method for positioning particles in a microchannel has garnered significant interest due to the relatively simple channel design compared to those typically used in hydrodynamic focusing methods. Although many theoretical and experimental results of inertial focusing have been published,

experimental analysis is typically done in 2D using methods such as microparticle streak velocimetry (μ-PSV)[26]. Work in characterizing 3D positioning in inertial focusing applications has been limited to confocal microscopy or stereoscopic microscopy[27, 28].

Our goal is to find a simple method of 3D tracking for micron-sized particles in focusing applications of varied Reynolds number. Particle defocusing methods, in which particles are imaged at varying vertical positions relative to the focal plane of the microscope so that their z-position is correlated to their apparent size, lends itself to a simple experimental setup. It has been shown previously that resolutions of several hundred nanometres are attainable using a defocusing method with a three-hole aperture design[29-31]. However, this method requires sophisticated understanding of optics and a custom aperture mask over the objective lens. Other calibration-based defocusing methods have been used without an aperture mask; however these methods typically require high-magnification/high-numerical aperture (*NA*) objective lens setups as they are reliant upon fitting the measured intensity profile to the point-spread function (PSF) of a single fluorescent particle[21, 32]. Diffraction ring defocusing methods such as this have become relatively commonplace, but little work has been done for larger particles (1-50 μm in size, equivalent to the size of most cells).

This paper describes the application of a defocusing-based 3D particle tracking technique to microfluidic particle focusing. The developed technique is based on calibration for typical microfluidic channel dimensions and finite Reynolds numbers (Re ≤ 100) with a high accuracy. Although our primary application is inertial focusing, this technique is also implemented to determine gravitational force effects to illustrate its use for a variety of experimental designs.

The following sections describe the experimental setup, theoretical background and two studies that were conducted to verify and validate the use of this method for particle focusing applications.

2. Experimental

2.1 Particle suspensions

All experiments used 15.5 μm (± 1.52 μm) green (emission wavelength = 502 nm) fluorescent polystyrene (PS) beads (Bangs Laboratories, CC FS07F, IN, USA). This size was chosen to mimic the size of many cells typically found in microfluidic assays including white blood cells and circulating tumour cells. Suspensions were provided at 1 wt%, and were diluted to 0.1 wt% using de-ionized (DI) water. 1 vol% of Tween-20 surfactant (Sigma-Aldrich, P1379, ON, Canada) was also added to these solutions to reduce particle aggregation.

2.2 Microfluidic device fabrication

Microfluidic devices were fabricated using soft lithography[33]. Lithography masters were fabricated at the Advanced Materials and Process Engineering Laboratory (AMPEL) Nanofabrication Facility (University of British Columbia) by first spin coating a 85 μm layer of SU-8 3050 (MicroChem, MA, USA) over 4-inch silicon wafers (University Wafer, MA, USA). The wafers were subsequently soft baked (95 ℃ for 40 minutes) and exposed to UV light (0.684 J/cm^2 at 400 nm) through a negative film mask (Qingyi Precision Maskmaking, Shenzhen, China). The wafers were then post-exposure baked (65 ℃ for 1 min, 95 ℃ for 5 min) and developed using SU-8 developer (MicroChem, MA, USA). Devices were then fabricated using the masters with poly(dimethylsiloxane) (PDMS) elastomer (Sylgard 184, Dow Corning, MI, USA). PDMS base and curing agent were mixed in a 10:1 ratio, spun to remove bubbles and poured over the masters. This was then baked (70 ℃, 1 h) and cooled before peeling the PDMS away from the master. This PDMS mould was then trimmed, with holes punched at the inlets and outlets. 75 x 50 x 1 mm No. 1 glass slides (VWR Scientific, PA, USA) are then cleaned with acetone, dried with N$_2$ gas and placed with the PDMS moulds into a plasma chamber (Harrick Plasma, NY, USA) where they are exposed (1 min 15 s) before being bonded and post-baked (70 ℃, 1 h). Syringe tips (.020 x .5 mm, NordsonEFD, OH, USA) are used as inlet and outlet feeds, secured and sealed using epoxy (ITW Devcon, MA, USA).

The microfluidic channel design used in these experiments was a simple 100 μm x 85 μm x 4 cm (W x H x L) rectangular straight channel, replicated several times on one wafer for reproducibility testing. Masters were checked for correct geometrical dimensions using a profilometer, with standard deviation σ_{width} = 1.2 μm and σ_{height} = 1.0 μm (Tencor AlphaStep 200, CA, USA). Consider Reynolds number,

$$Re = Q \frac{\rho_f}{\mu_f} \frac{D_H}{HW} \tag{1}$$

where Q is the applied flow rate, ρ_f is the fluid density, μ_f is the fluid viscosity, and H and W are the height and width of the channel respectively. The device cross-sectional area was chosen to approximate a 1:5 ratio of the particle diameter to the hydraulic diameter (D_H) of the channel, which from previous work has been shown to produce a variety of inertial focusing positions for particles across a range of Re[27, 34].

2.3 Fluorescence microscopy

2.3.1   Calibration curve using agarose gel suspension

In order to correlate the z-position of a particle in space to its apparent diameter, a calibration curve experimentally validating the relationship between these variables must be found. This was done using an agarose gel suspension of PS beads to hold particles in a randomly oriented distribution in space. The agarose suspension was made using DI water, 3 wt% agarose powder (Sigma-Aldrich, ON, Canada) and 0.1 wt% PS beads. This was mixed at 85 ℃ overnight (10 h) to ensure thorough incorporation of the gelling agent. By rapidly syringing this solution while still liquid into the microfluidic channels, the gel quickly solidified within the channel, keeping beads suspended at random z-positions within the channel boundaries.

Fig. 1a is a schematic of the experimental setup. The beads were imaged using fluorescence microscopy. A Nikon Eclipse
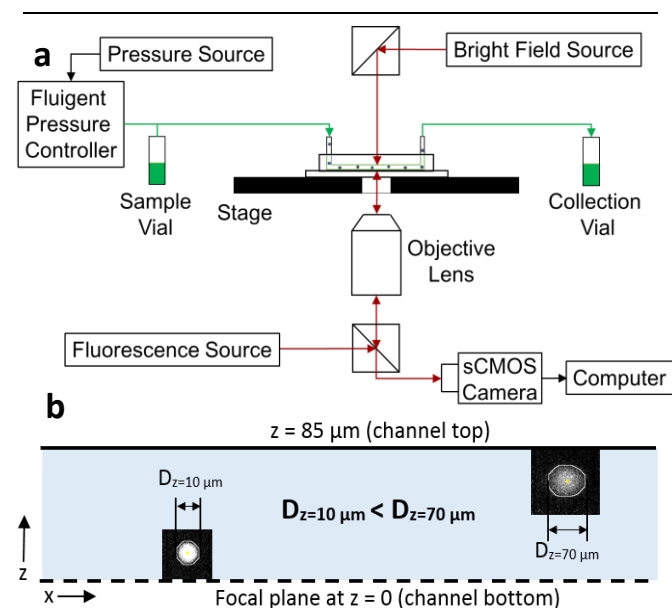

Fig. 1 Experimental schematic and general example of defocusing principle. (a) The experimental setup is simple, with few alterations from typical optical equipment. The microfluidic chip is placed on the stage, where both bright field (for finding the channel edges) and fluorescence sources (for imaging PS beads) are able to capture information. A filter cube (including a dichroic mirror and two filters for excitation (488 nm) and emission (507 nm), Nikon, Japan) is placed in-line with the fluorescence source and the sCMOS camera where image data is captured, collected using DaVis 7.2.2 software (LAVision, Göttingen, Germany) and sent to the computer for post-processing. The Fluigent pressure control system allows for precise control of flow rates (i.e. Re) from the sample vial through the microfluidic channel to the collection vial. Schematic is not to scale. (b) Focused particles maintain a diameter close to the actual diameter (15.5 ± 1.52 μm) while defocused particles have an intensity distribution spreading wider as they are positioned further from the focal plane. Therefore, with the focal plane at the bottom of the channel (z = 0), particles found closer to the top appear to be larger than those at the bottom. Two experimental examples are shown.

TE2000-U microscope was used, with a standard 10 X optical lens (Nikon Plan Fluor 10X/0.30, WD = 16 mm), $NA = 0.3$. A sCMOS camera (LAVision GmBH Imager sCMOS, MI, USA) with an exposure time of 100 μs was used to capture images of the beads in their varying positions. This exposure time was used for the calibration and all following experiments to give sufficient signal at a wide range of Re. Data was acquired using the suspended beads in three steps. First, the bottom of the channel was found and set as the $z = 0$ position in relation to the focal dial on the microscope. Then, the z-position from the bottom of the channel of each particle was determined with relation to the original position of the microscope's focal dial. Finally, each particle was imaged with the focal plane of the microscope at z = 0, thereby giving an apparent size value relative to its known z-position. Fig. 1b shows a general example of the defocusing effect on particle diameter. Z-position and particle data for each particle in the suspension was collected and a calibration curve of z-position and apparent particle diameter was made.

The following single-lens approximation equation was used as an adaptation of previously described work[35]:

$$d_e = M\left[d_p^2 + 1.49\lambda^2\left(\frac{n_o^2}{NA^2}-1\right) + 4z^2\left(\frac{n_o^2}{NA^2}-1\right)^{-1}\right]^{\frac{1}{2}} \quad (2)$$

where d_e is the expected/observed diameter of the particle, M is the magnification of the objective lens, λ is the wavelength of the fluorescence source, NA is the numerical aperture of the objective lens, z is the z-position of the particle with $z = 0$ as the origin, and n_o is the refractive index of the materials between the objective and the particle. Considering refraction occurs through the microfluidic channel (including the glass and PDMS substrates) and the solution medium before reaching the particle, $n_o = n_l/n_a$, $n_l = n_w/n_g$, $n_a = 1$, $n_w = 1.33$, $n_g = 1.52$ where n_l is refractive index of the chip (including fluid medium and glass) and n_a is the index of the air between the objective and the chip; magnification $M = 10$ as in previous work[36]. The equation above was derived under the assumptions of (1) uniform illumination in space, (2) a single thin-lens system and (3) particle image intensity distribution modelled as a Gaussian function[37]. We can include assumption (1) among the fulfilled requirements of our experimental setup, however we avoided using data collected from particles too close to the edges of the image frame, due to possible fringing effects from the illumination source at these locations. Considering assumption (2), a single-lens approximation does introduce error since our real microscope system is more complex. As identified in previous work, a more complex microscope system causes high error when a large magnification or large NA lens is used ($M \geq 20X$ and $NA \geq 0.4$)[35]. Manifestations of this error include a shift in the rate of defocusing (i.e. the slope of d_e related to z), an asymmetric defocusing pattern when considering objects above and below the focal plane, and possible optical distortions at the outer regions of the sCMOS image acquisition sensor. Our NA (0.3) and magnification (10X) are both below the values leading to

these error sources. Furthermore, because of the positioning of our focal plane at the bottom of the channel ($z = 0$), any asymmetric effects can be neglected since all of our objects will be physically above this plane ($z > 0$). As pertaining to assumption (3), although particles used in the justification of this single-lens equation ranged from $d_p = 1$ to 5 μm and our particles are slightly larger at $d_p = 15.5$ μm, a Gaussian approximation of the intensity distribution remains valid[37]. Many other defocusing methods use much smaller particles to experimentally determine the point-spread function (PSF) via diffraction ring patterns found in high magnification, high-NA images ($M = 20$ to 60X, $NA \geq 1$)[32, 38-40]. These diffraction patterns most closely resemble Bessel functions in shape. However, the intensity profile of larger particles can be approximated as a Gaussian function when viewed under relatively low magnification and NA[37, 41]. Considering all of the optical effects described, our experimental setup fits the assumptions used to derive equation (2). The calibration curve developed under these assumptions was used in all further experiments to relate apparent diameter of particles in flows to their vertical position in the channel.

2.3.2 Image acquisition

Data for all studies described in the Results section were collected using the same optical setup as the calibration curve with a standardized procedure. The microfluidic devices described in Section 2.2 are fitted with tubing of 0.5 mm inner diameter on the inlet and outlet. The inlet tubing was fit to a flow pressure control system (Fluigent MFCS-8C, Villejuif, France). The outlet was fed to a 2 mL collection vial. The bead solution described in Section 2.1 was fed through a T-junction into the inlet of the microfluidic channel at a known pressure dictated by the user through the Maesflo (v2.1.3) software accompanying the Fluigent system. A simple study was done to correlate pressure from the Fluigent to flow rate using a flow meter (Fluigent Flowell, Villejuif, France) (Fig. S1, Supplemental Information). Applied pressure can then be correlated to a given Reynolds number based on the following equation:

$$P_a(mbar) = 4.7088 \times 10^{12} \; Re \; \frac{\mu_f}{\rho_f}\frac{(2H + 2W)^2}{2W} \quad (3)$$

where Re is the Reynolds number, μ_f and ρ_f are the fluid viscosity and density, and H and W are the height (85 μm) and width (100 μm) of the channel. Beads then travel through the channel, where the sCMOS camera was positioned along its length (1 mm from the inlet for the gravitational force study (Section 3.2) and 1.5 cm from the inlet for the inertial focusing study (Section 3.3)) to acquire sets of images over time. The focal plane of the objective was always kept at the bottom plane of the channel (z = 0) to validate the use of the calibration curve in z-position determination later. The sCMOS camera captured 300 images at 30 Hz, for sets of 10 s time intervals. A number of data sets were collected in order to have at least several thousand (5000-10000) individual particle trajectories for each flow rate. This was done to reduce error based on initial position. Data sets were taken in several different channels with the same dimensions and

averaged. Data was acquired for $0.246 \leq Re \leq 75.356$. Particle image density ranged from 0-20 particles/image, with estimated displacement between frames of 50-2000 pixels depending on the chosen Re. Therefore, total number of data sets ranged from $5 - 50$ depending on the flow rate (Re), to have a total number of particles (data points) of at least 3000 for every flow rate.

2.4 Image post-processing

Once the data sets are acquired using the simple optical setup, each set was analysed using the free image software ImageJ and a custom MATLAB code to remove background. Specifically, a bright-field channel edge image was taken from each data set to determine the location of the channel edges within the frame. Then a background image was taken from each data set and is subtracted from each image containing particles. A spatial bandpass filter using a convolution of Gaussian and Boxcar functions was applied to each image to remove background noise and smooth the individual particle intensities. This code was developed prior to this work by John C. Crocker and David G. Grier[42]. This filter was supplemented with the MATLAB dilation and erosion functions to further resolve the edges of the each particle from the background. Finally, the MATLAB regionprops function was used to approximate the centroid location and equivalent diameter of each particle. A final overlay of the original image with the result of the image post-processing algorithm was used to visually confirm the accuracy of the method before a full image set was processed. Fig. 2 is a visual explanation of the entire image post-processing algorithm. The centroid and diameter data was then saved and compiled using Excel for each experimentally tested flow rate.

2.5 Particle tracking algorithm

The tracking algorithm used was originally developed by John C. Crocker and David G. Grier[42]. Given positions of n number of particles at a time t(i), and m possible new positions of the particles at a time t(i+1), the tracking algorithm considers all possible trajectories of the n old positions with the m new positions and chooses the trajectory which results in the minimal total squared displacement. Tracking individual particles can be used to determine individual particle velocity vectors or to more precisely understand conditions for particle displacement within the channel due to gravitational settling or other forces including inertial or fluid viscous drag.

3.   Results and discussion

3.1 Experimental error and uncertainty for calibration curve

The experimental results from the calibration curve were matched with the theoretical prediction from equation (2) and are shown in Fig. 3. Some previous work describes a linear trend between apparent diameter and z-position, whereas others have found a closer fit to equation (2)[21, 30, 35]. After completing an R^2 regression fit for a linear function and equation (2), $R^2_{linear} = 0.9045$ and $R^2_{(2)} = 0.9090$. We have decided to use equation (2) as a theoretical fit for our experimental data as it has a more thoroughly understood theoretical basis as discussed in Section 2.3.1[35].

As verified by the R^2 calculations, the experimental data has an error of 9.1% from equation (2). Coefficient of variation (CV = σ/μ; σ is the standard deviation, μ is the mean) was used to compare this experimental error with several hypothesized sources of uncertainty. Uncertainty is most likely attributable to several experimental steps related to human uncertainty. Each particle was deemed in focus based on observation through the microscope by eye, where a particle appears to be the smallest diameter compared to its size at any other focal plane. To determine a quantitative measure of this uncertainty, the same particle was observed and brought into focus 10 times. Standard deviation of this observed in-focus position was 1.3 μm (CV = 8.4%). Another source of uncertainty could be related to
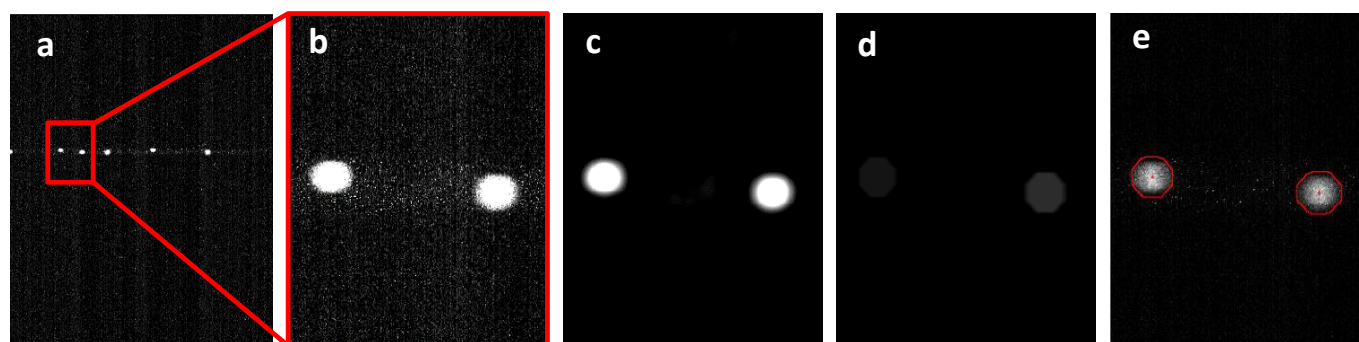

Fig. 2 Visualization of image post-processing algorithm. (a) An original image from the sCMOS camera is imported into MATLAB. The following images (b-e) are of a zoomed-in portion of the total image to emphasize the effect of the algorithm. (b) A zoomed-in portion of the total image, no post-processing conducted at this step. (c) A bandpass filter, including a convolution of Gaussian and Boxcar (a dual-sided Heaviside) functions, is used to remove background noise and better resolve the edges of the beads. (d) Dilation and erosion functions embedded in MATLAB are used to approximate the finite edges of the beads (an octahedral geometry is used rather than a higher-sided shape to reduce computational time). (e) The results of the dilation/erosion functions are mapped using regionprops and overlaid over the original image to verify accuracy of the algorithm. One image is checked in this manner for each image set before the algorithm is run for all 300 images in the set.
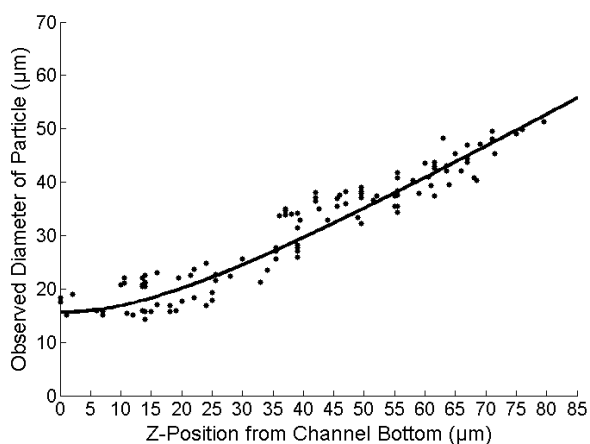
Fig. 3 Calibration data and theoretical curve relating z-position of a particle in the channel to its observed diameter. As predicted from equation (2), the observed diameter of the particles (mean observed diameter = 30.82 μm) steadily increases with increasing distance from the focal plane (at z = 0). $R^2 = 0.9090$.

the standard deviation of the particle size ($\pm$ 1.52 μm, CV = 9.8%). Since each particle has a slightly different size, two particles at the same z-position can have differing apparent diameters. This is apparent from the experimental data shown in Fig. 3. Notably, particles with the same z-position have CV = 7.3%, which falls within the uncertainty described above. While the manufacture of particles could be altered based on more stringent production specifications, the human source of uncertainty is unavoidable and restricts the use of this experimental technique to particles larger than the human factor uncertainty (approximately 2 μm).

3.2 Consideration of peak-locking effects in image post-processing algorithm

It has been noted in several PIV and particle tracking velocimetry (PTV) works that error can be caused by a sub-pixel resolution issue known as peak-locking[43-45]. In many image processing algorithms, particle diameter and centroid positions are calculated based on an approximation to the closest pixel along the edge (in the case of diameter) or in the centre of the particle (in the case of centroid determination). This error is especially prevalent in cases where the particles are close to the size of individual pixels in the image. Due to the large size of the particles and high resolution of the images, each particle is approximately 35-40 pixels in diameter. Therefore, error associated with peak-locking would be on the order of 2-3%. As a thorough confirmation for all Re considered in our experiments, a 2D histogram plot (Fig. S2, Supplemental Information) of the probability density function (PDF) of the sub-pixel centroid positions, as well as a 1D histogram plot (Fig. S3, Supplemental Information) of the sub-pixel part of the diameter were made. Notably, there is no discernible peak-locking effects in these analyses, which confirms that this image post-processing algorithm is viable for our technique.

3.3 Effects of gravitational force on low Re flows discernible to 1-μm resolution

A great deal of work has been done to investigate the effects of inertial forces on particle positioning in channels[34, 46-49]. However, most studies have been done using non-density-matched particles without taking into account the possible effects of gravitational forces on their positions. Therefore this study acts as a validation of our method of vertical position while developing a more thorough understanding of the forces affecting particle positioning.

Centroid and diameter data was collected for particles for $0.246 \leq Re \leq 1.237$. The tracking algorithm was implemented across frames in each 300-image data set. Particles that have been imaged at both the far-left (within the first 50 pixels, excluding the first 10 pixels following assumption (2) for eq. (2)) and far right (within the last 50 pixels, excluding the last 10 pixels) of the frame were tallied and their change in diameter was monitored. The channel walls were carefully oriented perpendicular to the camera frame to avoid particle initial position affecting particle travel length across the channel. The overall change across the frame length (1.35 mm) was then determined for each particle and results are averaged over the total number of particles observed.

In order to complete the validation, a theoretical analysis of the settling effects of gravitational forces on particles in the flow must be prepared and compared to the experimental results. Three forces are considered: gravitational (F_g), buoyancy (F_b) and Stokes drag force of the particles relative to the medium flow (F_D).

$$F_g - F_b - F_D = m_p \frac{du_p}{dt} \quad (4)$$

with,

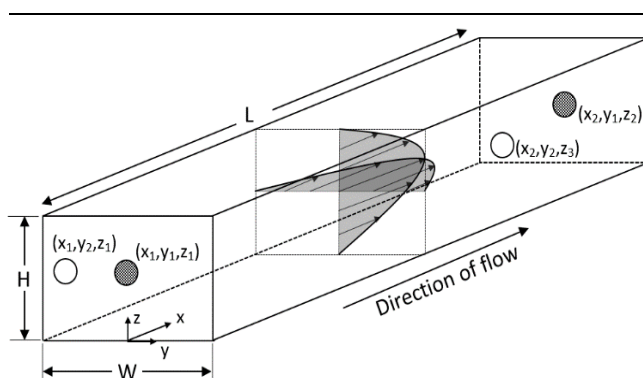$$F_g = \rho_p V g \quad (5)$$

$$F_b = \rho_f V g \quad (6)$$

Fig. 4 Illustration of the double-parabolic velocity profile. The fluid velocity profile in a rectangular channel can be approximated as a double-parabola for two axes (y,z). Since the highest fluid velocity is found in the centre of the channel, the particle velocity will also be highest at this position. Therefore, particle settling will be lowest for a particle initial position (x,y,z) = (x,0,H/2), and increase as particles are initially positioned closer to the channel walls. The initial and final positions of the two particles are illustrated. $x_1 = 0$, $x_2 = 1.35$ mm downstream (the width of a capture frame).

$$F_D = 3\pi\mu d_p U_p \qquad (7)$$

Integration of (4) leads to the following result:

$$u_z(t) = u_\infty \left(1 - e^{\frac{-t}{\tau}}\right) \qquad (8)$$

$$u_\infty = \frac{g(\rho_p - \rho_f)d_p^2}{18\mu} \qquad (9)$$

$$\tau = \frac{\rho_p d_p^2}{18\mu} \qquad (10)$$

where ρ_p is the particle density, ρ_f is the fluid density, μ is the fluid viscosity, g is the gravitational acceleration, d_p is the particle diameter, V is the particle volume, u_∞ is the steady-state sedimentation velocity in the z-direction, u_z is the sedimentation velocity in the z-direction, and τ is a time constant related to the particle's motion in the fluid. For our particular geometry, τ = 16.84 µs and u_∞ = 10.60 µm/s. Therefore, within approximately 17 µs, $u_p \approx u_\infty$.

The above result can be used to relate the particle's initial (x,y,z) coordinates in space to its final position 1.35 mm downstream, with the sedimentation velocity approximately equal to u_∞. Using the first approximation of first-order Ritz velocity profile, the x-component velocity distribution in non-dimensional form is obtained as[50]:

$$u_x(\Delta z) = \frac{dx}{dt}(\Delta z) = \frac{9}{4}\frac{Q}{HW}\left(1 - 4\left(\frac{y_o}{W}\right)^2\right)\left(1 - 4\left(\frac{z_o + \Delta z}{H}\right)^2\right) \qquad (10)$$

The y-position is considered constant ($u_y \approx 0$) as there are no forces acting along the y-axis during flow to shift particles along this direction. Experimental results confirmed this assumption, as particles tend to shift within 1 µm along the y-axis over the length of the frame. However, particles that begin at a y-position closer to the walls of the channel will have a final position closer to z = 0 than particles with an initial y-position closer to the centre of the channel (Fig. 4). This is due to the double-parabolic velocity profile within a rectangular microfluidic channel. Integration of dx/dt over t and application of height and width constants (de-normalization) for the y and z terms leads to this final relationship between a particle's x and z positions within the channel:

$$x = \frac{81Q\mu}{2g(\rho_p - \rho_f)HWd_p^2}\left(1 - 4\left(\frac{y_o}{W}\right)^2\right)\left(\Delta z - \frac{4}{3H^2}[(z_o + \Delta z)^3 - z_o^3]\right) \qquad (11)$$

where Q is the input flow rate decided by the user and H and W are the height and width of the channel, respectively. Fig. 5 shows this relationship for a selection of the Re chosen from the experimental procedure. Although this is a third-order polynomial, the $(x, \Delta z)$ relationship approximates linearly. This is because for x ≤ 1.35 mm, Δz reaches a maximum of approximately 5 µm, while H = 85 µm. Therefore, $(\Delta z/H)^3 << (\Delta z/H)$. Fig. 6 combines the theoretical and experimental results for gravitational settling. In general, the
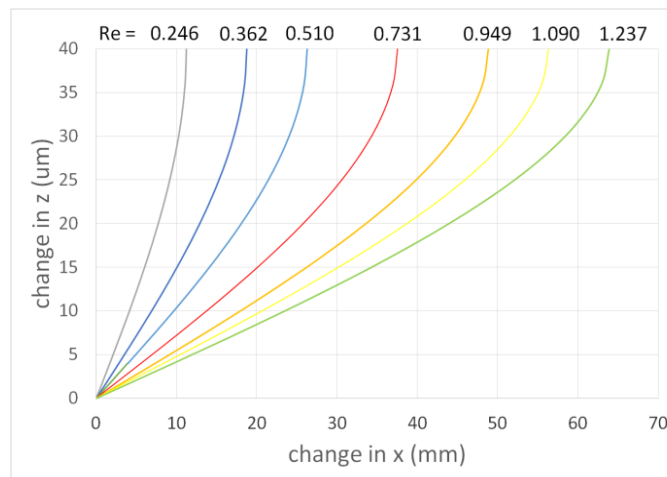

Fig. 5 Cubic relationship between change in x and change in z due to settling. These are results analytically derived from equation (11). The relationship is indeed cubic, however, for small changes in x (as in our case, where Δx_{max} = 1.35 mm), the relationship can be approximated linearly. In general, the higher the Reynolds number, the higher the flow rate, and therefore the lower the change in z across a change in x.

experimental results match well with predicted theoretical trends of settling across the channel. Experiments show a change in z of 0.5-3.5 µm across the frame length. This is associated with a 2-5 µm diameter change (~3-8 pixels) depending on the particle's initial position. Experimental value uncertainty increases in general with increasing Reynolds number. This is reasonable considering that increased initial flow rate pushes particles into the walls, creating a more random initial distribution.

The effect of gravity on particle positions becomes relatively small as Re increases above 1 for our system ($\Delta z \leq 0.05(d_p)$). Therefore, most previous work is sound in that flow rates are typically much higher and therefore the lift forces related to
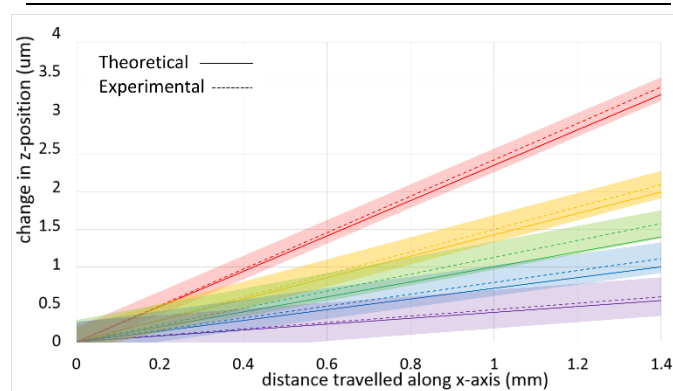

Fig. 6 Theoretical and experimental settling study results. Results are illustrated as simple lines and error bars are illustrated using semi-transparent zones as results are averaged across many particles (100-1000 depending on the pressure chosen). As expected, an increase in Reynolds number causes a decrease in overall settling. Most importantly however, experimental results are within 1 µm of the theoretical prediction for each Reynolds number (i.e. applied pressure) chosen. Uncertainty (shown as coloured bands) ranges from ± 0.2 µm to ± 0.39 µm from the average slopes, increasing with increasing Reynolds number.

inertial effects become predominant. However, the regime in which gravitational forces are of an equivalent order to the other forces acting on particles in microfluidic flows could be used to create unique focusing positions. The gravitational settling work was used to verify that defocusing can be used for 3D tracking of moving particles in a microfluidic channel.

3.4 Inertial focusing positions of particles distinguishable using defocusing method

A second set of data was collected over a wider range of flow rates (1 − 330 μL/min (0.246 ≤ Re ≤ 75.356)) to determine experimental focusing positions of particles due to inertial effects. This is an important application of our method, as many researchers working in this area wish to have a complete 3D understanding of the particle positioning without a complex experimental setup or post-processing algorithm. In inertial focusing, particles reach equilibrium positions based on the balance of two dominant forces: the viscous drag (F_D) which sends particles along fluid streamlines, and the inertial lift force (F_L) that leads particles to migrate across streamlines. The inertial lift force can be further separated into a wall-induced lift force (F_W) which acts away from the wall of the channel towards the center, and a shear-induced lift force (F_s) that acts towards the channel walls. The net lift force is responsible for the final equilibrium position of the particles[34]. If the geometry is a rectangular channel, high flow rates cause a 6-point symmetrical convergence of particles close to the centre of each of the two longer walls of the channel and the four corners[26, 34, 51-53]. The

particles then tend to migrate to a 2-point equilibrium depending on how far down the channel the particles have travelled[54]. Fig. 7a is an illustration of the overall inertial focusing effect conjectured for our specific cross-sectional channel geometry.

Following a procedure similar to that outlined in Section 3.1, image sets were collected in various channels at a position 1.5 cm from the channel inlet and particle trajectories were found using the tracking algorithm. 2D plots of the cross-section of the channel were developed using MATLAB to map particle positions at varying flow rates. Due to the density of particles in specific regions in these plots, the data was converted to a probability density plot using a PDF. The PDF is derived by determining the number of particles found in partitioned bins of the 85 x 100 μm channel cross-section. These values are then normalized by the bin with the highest number of particles. Fig. 7b shows the results from the 7 flow rates chosen for this study. These flow rates (Re) were chosen as they have been previously used to identify unique focusing positions of particles in square or rectangular channels[27, 34].

As shown in Fig. 7, the particles tend to migrate away from the center of the channel towards the walls along the y-axis, also spreading towards the top and bottom walls at higher flow rates. This generally follows trends indicated from previous work; however, particles tend to stay along the central vertical plane rather than migrating towards the top and bottom walls. Also, there is an oval-shaped particle distribution between 10 ≤ Re ≤ 35. This distribution has not previously been described[26, 27, 34, 46], and may represent an intermediate focusing
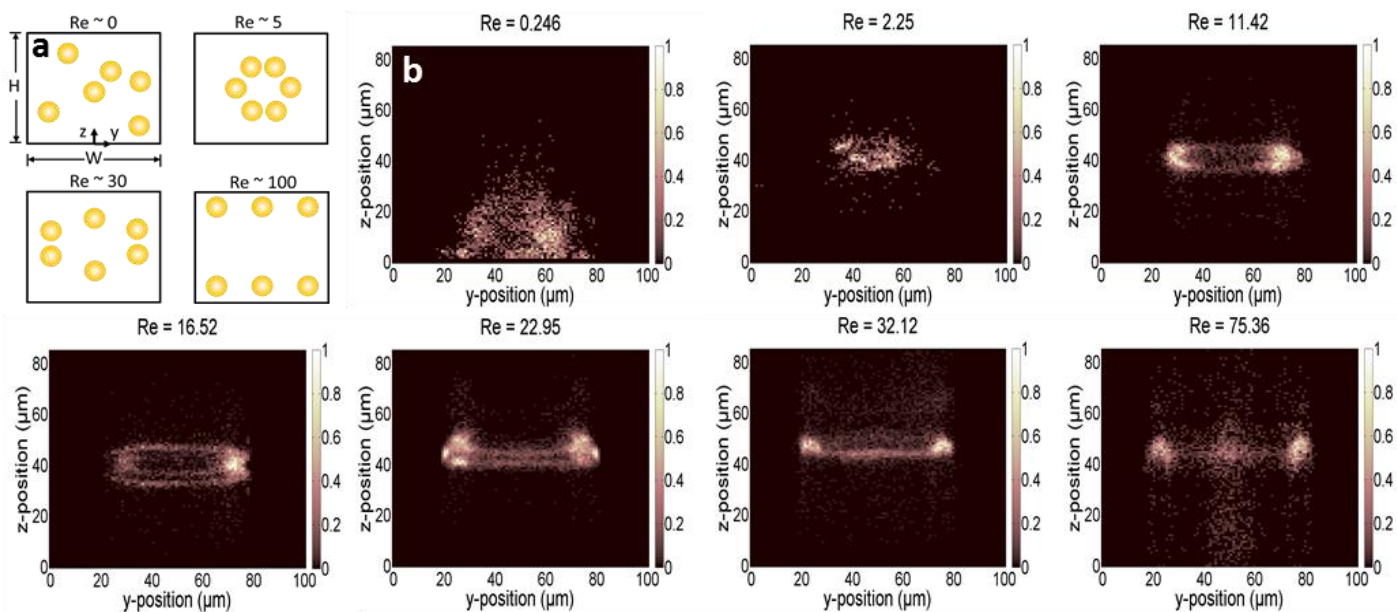

Fig. 7 Conjectured and experimental focusing trends for particles in a rectangular channel (a) A schematic of the predicted trend for inertial focusing of particles in our rectangular channel geometry. Particles begin in the centre of the channel and move outward towards the walls with increasing Reynolds number. Due to the aspect ratio of a rectangular channel, particles are predicted to focus towards 4-6 positions at the top and bottom of the channel for high Reynolds number. (b) Probability density contour plots of experimental data for inertial focusing using the defocusing method. Particles are initially found at the bottom of the channel, due to low applied pressure and the effect of gravitational settling as discussed in Fig. 5-7. As Reynolds number increases, particles form a circular cross-section in the channel, slowly shifting away from the center and spreading outward. Eventually (Re = 75.356), particles appear to be mainly positioned in 4 positions towards the middle of each wall, with some particles maintaining positions near the center of the channel. Each cross-section was split into 100 x 100 bins (bin size of 1 x 0.85 μm). The color bar values indicate a normalization of the number of particles found within each bin (0 indicating no beads found, 1 indicating the maximum number of beads found across the entire cross-section).

regime between unfocused particles and particles focused towards the walls as indicated in Fig. 7a. Finally, we compare our results and method to those previously used in inertial microfluidics. Typically, only 2D results are used to validate inertial effects experimentally, the most common of which is μ-PSV[34, 54]. However, 2D methods such as this give little understanding of individual particle trajectories, or vertical positioning information. Furthermore, 2D methods are difficult to normalize, as they are reliant on average intensity of many hundreds of particles viewed in a channel. The simple 3D method demonstrated here allows for individual particle tracking to create an overall cross-section of particle positioning in the channel as seen in Fig. 7b.

4. Conclusions

This paper describes the use of a calibration-based defocusing method for three-dimensional particle tracking and particle velocimetry in a microscale flow volume for particle focusing applications. The developed technique provides a convenient means of determining particle locations, specifically along the vertical axis, in microscale flows. The method can be easily translated to a variety of optical systems without custom lenses, apertures, added cameras or optical pieces such as prisms or beam separators. Effects of gravitational forces on low Re flows are discernible to 1 μm resolution. Based on the particle positions determined from this method, three-dimensional particle velocity vectors could be calculated. This method is designed specifically for micron-sized particles such as cells and other particles (i.e. bacteria); however it could also be used, with higher *NA* and higher magnification objectives, in μPIV applications to better understand specific microflows such as microreactors or mixers.

By automating the calibration, this method could be used to track particles less than 2 μm in diameter. Future work will explore use of this technique with biological samples[53], and as a method for determining unique Reynolds number regimes for controlling particle flows for separation by density, size, morphology, or biochemical characteristics.

Acknowledgements

Notes and References

[a] Electrical & Computer Engineering, University of British Columbia, 3064 – 2332 Main Mall, Vancouver, British Columbia V6T 1Z4, Canada. E-mail: mwiner@ece.ubc.ca; Tel: +1 604 827 4114

[b] Mechanical Engineering, University of British Columbia Okanagan, 1137 Alumni Ave, Kelowna, British Columbia V1V 1V7, Canada.

E-mail: aahmadi@ece.ubc.ca

1. J. G. Santiago, S. T. Wereley, C. D. Meinhart, D. J. Beebe and R. J. Adrian, *Exp Fluids*, 1998, **25**, 316-319.
2. S. T. Wereley and C. D. Meinhart, *Annual Review of Fluid Mechanics*, 2010, **42**, 557-576.
3. T. Hirono, H. Arimoto, S. Okawa and Y. Yamada, *Measurement Science and Technology*, 2008, **19**, 025401.
4. C. D. Meinhart, S. T. Wereley and J. G. Santiago, *Exp Fluids*, 1999, **27**, 414-419.
5. A. Yildiz, J. N. Forkey, S. A. McKinney, T. Ha, Y. E. Goldman and P. R. Selvin, *Science*, 2003, **300**, 2061-2065.
6. F. Scarano, *Measurement Science and Technology*, 2013, **24**, 012001.
7. G. Sina and S. Fulvio, *Measurement Science and Technology*, 2010, **21**, 127002.
8. N. Matteo, B. Kees Joost and S. Fulvio, *Measurement Science and Technology*, 2010, **21**, 035401.
9. W. Bernhard, *Measurement Science and Technology*, 2013, **24**, 024008.
10. S. A. Klein, J. L. Moran, D. H. Frakes and J. D. Posner, *Measurement Science and Technology*, 2012, **23**, 085304.
11. J.-B. Sibarita, in *Microscopy Techniques*, ed. J. Rietdorf, Springer Berlin Heidelberg, 2005, vol. 95, pp. 201-243.
12. C. Cierpka, M. Rossi, R. Segura and C. J. Kähler, *Measurement Science and Technology*, 2011, **22**, 015401.
13. M. Hui, P. Gang, P. Ye and H. W. Scott, *Measurement Science and Technology*, 2004, **15**, 673.
14. R. Lindken, J. Westerweel and B. Wieneke, *Exp Fluids*, 2006, **41**, 161-171.
15. C. Cierpka and C. J. Kähler, *Journal of Visualization*, 2012, **15**, 1-31.
16. S. Lee and S. Kim, *Microfluid Nanofluid*, 2009, **6**, 577-588.
17. S. Williams, C. Park and S. Wereley, *Microfluid Nanofluid*, 2010, **8**, 709-726.
18. F. Pereira, J. Lu, E. Castaño-Graff and M. Gharib, *Exp Fluids*, 2007, **42**, 589-599.
19. G. E. Elsinga, F. Scarano, B. Wieneke and B. W. Oudheusden, *Exp Fluids*, 2006, **41**, 933-947.
20. H. Kim, S. Große, G. Elsinga and J. Westerweel, *Exp Fluids*, 2011, **51**, 395-405.
21. J. S. Park and K. D. Kihm, *Exp Fluids*, 2006, **40**, 491-499.
22. E. Toprak, H. Balci, B. H. Blehm and P. R. Selvin, *Nano Letters*, 2007, **7**, 2043-2045.
23. O. Dron and J. L. Aider, *EPL (Europhysics Letters)*, 2012, **97**, 44011.
24. P. B. Muller, M. Rossi, Á. G. Marín, R. Barnkob, P. Augustsson, T. Laurell, C. J. Kähler and H. Bruus, *Physical Review E*, 2013, **88**, 023006.
25. T. Fuchs, R. Hain and C. Kahler, in *10th International Symposium on Particle Image Velocimetry*, Delft, The Netherlands, 2013.
26. A. A. S. Bhagat, S. S. Kuntaegowdanahalli and I. Papautsky, *Physics of Fluids*, 2008, **20**, 101702-101704.
27. D. Di Carlo, D. Irimia, R. G. Tompkins and M. Toner, *Proceedings of the National Academy of Sciences*, 2007, **104**, 18892-18897.
28. D. Di Carlo, J. F. Edd, K. J. Humphry, H. A. Stone and M. Toner, *Physical Review Letters*, 2009, **102**, 094503.

29. C. E. Willert and M. Gharib, *Exp Fluids*, 1992, **12**, 353-358.
30. S. Y. Yoon and K. C. Kim, *Measurement Science and Technology*, 2006, **17**, 2897.
31. K. Kim, *Journal of Mechanical Science and Technology*, 2012, **26**, 3769-3784.
32. M. Speidel, A. Joná and E.-L. Florin, *Opt. Lett.*, 2003, **28**, 69-71.
33. D. C. Duffy, J. C. McDonald, O. J. A. Schueller and G. M. Whitesides, *Analytical Chemistry*, 1998, **70**, 4974-4984.
34. A. Bhagat, S. Kuntaegowdanahalli and I. Papautsky, *Microfluid Nanofluid*, 2009, **7**, 217-226.
35. M. Rossi, R. Segura, C. Cierpka and C. Kähler, *Exp Fluids*, 2012, **52**, 1063-1075.
36. J. B. Christopher, G. O. Michael and A. D. Gorby, *Measurement Science and Technology*, 2004, **15**, 318.
37. M. G. Olsen and R. J. Adrian, *Exp Fluids*, 2000, **29**, S166-S174.
38. J. G. McNally, T. Karpova, J. Cooper and J. A. Conchello, *Methods*, 1999, **19**, 373-385.
39. F. Gibson Sf Fau - Lanni and F. Lanni, 1991.
40. J. S. Park, C. K. Choi and K. D. Kihm, *Measurement Science and Technology*, 2005, **16**, 1418.
41. R. J. Adrian and C.-S. Yao, *Applied Optics*, 1985, **24**, 44-52.
42. J. C. Crocker and D. G. Grier, *Journal of Colloid and Interface Science*, 1996, **179**, 298-310.
43. J. Chen and J. Katz, *Measurement Science and Technology*, 2005, **16**, 1605.
44. L. B. Fore, *Measurement Science and Technology*, 2010, **21**, 035402.
45. K. P. Angele and B. Muhammad-Klingmann, *Exp Fluids*, 2005, **38**, 341-347.
46. D. Di Carlo, *Lab on a Chip*, 2009, **9**, 3038-3046.
47. J.-S. Park, S.-H. Song and H.-I. Jung, *Lab on a Chip*, 2009, **9**, 939-948.
48. S. S. Kuntaegowdanahalli, A. A. S. Bhagat, G. Kumar and I. Papautsky, *Lab on a Chip*, 2009, **9**, 2973-2980.
49. Z. Wu, B. Willing, J. Bjerketorp, J. K. Jansson and K. Hjort, *Lab on a Chip*, 2009, **9**, 1193-1199.
50. B. Kundu, S. Simlandi and P. Das, *Heat Mass Transfer*, 2011, **47**, 1289-1299.
51. Y. W. Kim and J. Y. Yoo, *Journal of Micromechanics and Microengineering*, 2008, **18**, 065015.
52. B. Chun and A. J. C. Ladd, *Physics of Fluids*, 2006, **18**, 031704.
53. E. J. Lim, T. J. Ober, J. F. Edd, G. H. McKinley and M. Toner, *Lab on a Chip*, 2012, **12**, 2199-2210.
54. J. Zhou and I. Papautsky, *Lab on a Chip*, 2013, **13**, 1121-1132.